OPTICA

High-speed 4D fluorescence light field tomography of whole freely moving organisms

Kevin C. Zhou,[1,2,*] Clare Cook,[1] Archan Chakraborty,[3] Jennifer Bagwell,[4] Joakim Jönsson,[1] Kyung Chul Lee,[1] Xi Yang,[1] Shiqi Xu,[1] Ramana Balla,[1] Kushal Kolar,[5] Caitlin Lewis,[6] Mark Harfouche,[7] Donald T. Fox,[3] Michel Bagnat,[4] and Roarke Horstmeyer[1,8]

[1]Department of Biomedical Engineering, Duke University, Durham, North Carolina, USA
[2]Department of Biomedical Engineering, University of Michigan, Ann Arbor, Michigan, USA
[3]Department of Pharmacology & Cancer Biology, Duke University, Durham, North Carolina, USA
[4]Department of Cell Biology, Duke University, Durham, North Carolina, USA
[5]Department of Biomedical Engineering, Tandon School of Engineering, New York University, Brooklyn, New York, USA
[6]Department of Electrical & Computer Engineering, Duke University, Durham, North Carolina, USA
[7]Ramona Optics Inc., 1000 W Main St., Durham, North Carolina 27701, USA
[8]roarke.w.horstmeyer@duke.edu
*kczhou@umich.edu

Received 21 November 2024; revised 30 March 2025; accepted 3 April 2025; published 5 May 2025

Volumetric fluorescence imaging techniques, such as confocal, multiphoton, light sheet, and light field microscopy, have become indispensable tools across a wide range of cellular, developmental, and neurobiological applications. However, it is difficult to scale such techniques to the large 3D fields of view (FOV), volume rates, and synchronicity requirements for high-resolution 4D imaging of freely behaving organisms. Here, we present reflective Fourier light field computed tomography (ReFLeCT), a high-speed volumetric fluorescence computational imaging technique. ReFLeCT synchronously captures entire tomograms of multiple unrestrained, unanesthetized model organisms across multi-millimeter 3D FOVs at 120 volumes per second. In particular, we applied ReFLeCT to reconstruct 4D videos of fluorescently labeled zebrafish and *Drosophila* larvae, enabling us to study their heartbeat, fin and tail motion, gaze, jaw motion, and muscle contractions with nearly isotropic 3D resolution while they are freely moving. To our knowledge, as a novel approach for snapshot tomographic capture, ReFLeCT is a major advance toward bridging the gap between current volumetric fluorescence microscopy techniques and macroscopic behavioral imaging.

https://doi.org/10.1364/OPTICA.549707

1. INTRODUCTION

Non-invasive tomographic 3D imaging has revolutionized basic scientific and medical research by revealing the internal structure of thick, volumetric specimens in their native biological context. However, dense tomographic 3D imaging over large fields of view (FOVs) requires a very large number of spatially resolved measurements—orders of magnitude more data than 2D imaging. As a result, without increasing the acquisition bandwidth, the volume rate must be sacrificed in order to fully sample the 3D volume. It is thus challenging to perform volumetric imaging of highly dynamic organisms without motion artifacts, especially as the 3D FOV increases. To perform 3D tomographic imaging of whole organisms, one generally must resort to chemical fixation, immobilization, or movement restraint, which disturbs the organism's natural physiological state. An ideal tomographic imaging system would be able to synchronously capture 3D measurements of entire dynamic specimens in a single snapshot to minimize motion artifacts. Apart from avoiding the confounding effects of immobilization, such a capability would also open up new scientific opportunities for jointly observing organism behavior, morphology, and fluorescent activity, all seamlessly across 3D space and time.

Point-scanning techniques such as confocal microscopy [1] and multiphoton microscopy [2], as well as parallelized versions [3,4], are often too slow to image dynamic samples, due to the need to perform inertially constrained scanning of focused points in three dimensions. The inherent asynchrony of the acquisition of the 3D points comprising the volume of view leads to "rolling shutter" artifacts. Point-scanning techniques also tend to require high-focused laser intensities, as the per-pixel integration time decreases with increasing frame or volume rate. Light sheet microscopy techniques have alleviated many of these limitations and achieved impressive volumetric imaging rates owing to their high-speed parallel 2D detection [5–14]. However, they still require mechanical scanning in one dimension, thus imposing an inverse relationship between volume rate and the number of depth planes,

which are acquired asynchronously. Further, at a fixed volume rate, the focused intensity of the light sheet must increase with the number of depth planes to achieve the same SNR. Light sheet and point-scanning microscopy approaches alike also typically have limited FOVs and thus often require organism immobilization.

Computational reconstruction techniques such as those used in optical projection tomography (OPT) [15] and optical diffraction tomography (ODT) [16,17] traditionally require sequential acquisition of hundreds of multi-angle images, which compromises speed, especially if mechanical translation or rotation is required. Multiplexing and compressive sensing can reduce the number of acquisitions and thus increase imaging speed [18,19], albeit at the cost of reconstruction quality. Optical coherence tomography (OCT) [20,21] is another class of wide-FOV, high-speed volumetric imaging. Even as faster sources pushing multi-MHz A-scan rates are being developed [22], OCT is also constrained by lateral mechanical scanning speeds and a lack of functional image contrast.

On the other hand, light field microscopy (LFM) and related techniques [23–28] capture 3D information synchronously in a single snapshot, requiring no moving parts. However, the light field information must be encoded on a 2D sensor, whose limited bandwidth imposes a tradeoff not only between spatial and angular information but also temporal sampling. 3D techniques that perform data undersampling and use compressive sensing techniques can help address some of these shortcomings [26,29]. While useful in certain applications, these methods often rely on strong regularizers or priors that can erase features and are not applicable when sparsity assumptions are not met. Additionally, the 3D reconstruction quality is limited by the missing cone problem due to practical design constraints of the refractive objective lens, on which most LFM designs are based, that restrict the angular coverage to less than 2π steradians. A further complication of practical refractive objective lens designs is that achieving larger angular coverage [i.e., high numerical aperture (NA)] comes at the cost of field of view (FOV) and working distance, rendering imaging of freely behaving organisms challenging.

Here, we present a new type of high-throughput computational tomographic imaging technique based on a reflective Fourier light field design that allows for super-video-rate volumetric imaging of unrestrained organisms (e.g., freely swimming zebrafish and fruit fly larvae) over tens-of-cubic-millimeter FOVs (Fig. 1; Visualization 1). Key to our design is a reflective concave mirror, which overcomes many limitations of refractive objectives, enabling high angular coverage that can approach 4π steradians [30] with large working distances [31]. In particular, our design combines a reflective parabolic mirror objective [32] with an array of 54 individual cameras to synchronously acquire videos from multiple views distributed across nearly 2π steradians at up to 120 Hz (multiple gigavoxels/s). We call our method Reflective Fourier Light field Computed Tomography (ReFLeCT), which we applied to perform fluorescence imaging of several freely moving zebrafish and fruit fly larvae. Our algorithm reconstructs not only the 3D fluorescence distribution of the sample but also its 3D optical attenuation map, which is possible due to the extreme angular coverage of ReFLeCT. To account for rapid changes in animal position and orientation throughout the videos, we developed a tracking and registration algorithm that enables fully 3D observation of physiological properties (e.g., morphological dynamics, eye movement, and cardiac function) that would otherwise require immobilizing the animal to accurately record. We also demonstrate multi-organism imaging [Fig. 1(c), Fig. S3 in Supplement 1, Visualization 4, Visualization 5, and Visualization 6], opening the door to high-speed volumetric imaging of behavioral interactions among multi-mm-sized organisms [33–37].

2. REFLECTIVE FOURIER LIGHT FIELD COMPUTED TOMOGRAPHY (ReFLeCT)

A. Concept and Design

ReFLeCT combines a parabolic mirror with a multi-camera array architecture, thereby enabling snapshot multi-view spatioangular sampling of a given volume of interest with significantly higher sampling than conventional Fourier light field microscopes (Fig. 1; Visualization 1). Working backward from the plane of image capture, the ReFLeCT system consists of an array of 54 RGB camera sensors (ONSemi AR1335, 3120×4208 pixels each, 1.1 μm pitch) arranged in a 9 by 6 grid, with a center-to-center camera spacing of $p = 13.5$ mm (Ramona Optics Inc.). We are able to stream data from the entire array (up to 700 megapixels per snapshot, synchronized across all 54 image sensors) to computer memory at rates exceeding 5 GB/s. We operated the sensors at $2\times$ or $4\times$ downsampling to achieve 30 and 120 fps frame rates, respectively.

Each camera sensor has an identical lens (Edmund Optics), whose principal planes are approximately a focal length distance f_{lens} away so that the object planes are at infinity. Another focal length distance below the lens principal planes (i.e., the Fourier planes) is an array of circular apertures, which serve as aperture stops that define the lateral resolution and depth of field (DOF) of the system's acquired multiview images (Section 2.2). Between the apertures and lenses is an array of bandpass emission filters (Chroma, 530/50 nm) for green fluorescence imaging. Finally, below these arrays is a large, rotationally symmetric parabolic mirror (Optiforms, Inc.) with an $f_{\text{mirror}} = 25.4$ mm focal length and 141 mm diameter aperture, which acts as a common reflective objective for all 54 cameras. Thus, the 54 camera lenses can be thought of as tube lenses, forming nearly 4f imaging systems with the parabolic mirror acting as the primary objective lens, thereby enabling multi-view imaging spanning $\sim 2\pi$ steradians of a sample placed at the focus of the mirror. The sample is illuminated through a 12.7 mm diameter hole at the apex of the parabolic mirror with a blue LED (Thorlabs, $\lambda = 455$ nm) with a 500 nm short-pass excitation filter (Thorlabs). The sample holder is an important design consideration for the imaging system, as it not only holds the sample and impacts the FOV but also influences the image quality, as it acts as the first optical element of the ReFLeCT system after the sample (see Section 2.3). Ideally, the sample holder is a spherical shell with uniform thickness (i.e., an optical dome), which introduces minimal aberrations and allows unobstructed observation from any view angle [30]. To this end, we adopt tubes designed for chemical analysis by nuclear magnetic resonance (NMR) spectroscopy, which have hemispherical bottoms that transition into a cylindrical shaft and are produced to have as uniform wall thickness as possible to avoid wobble while spinning. The inner diameter of the tube is ~3.43 mm, which determines the maximum possible FOV. The effects of the NMR tube are accounted for in our forward model (Note 2C in Supplement 1).

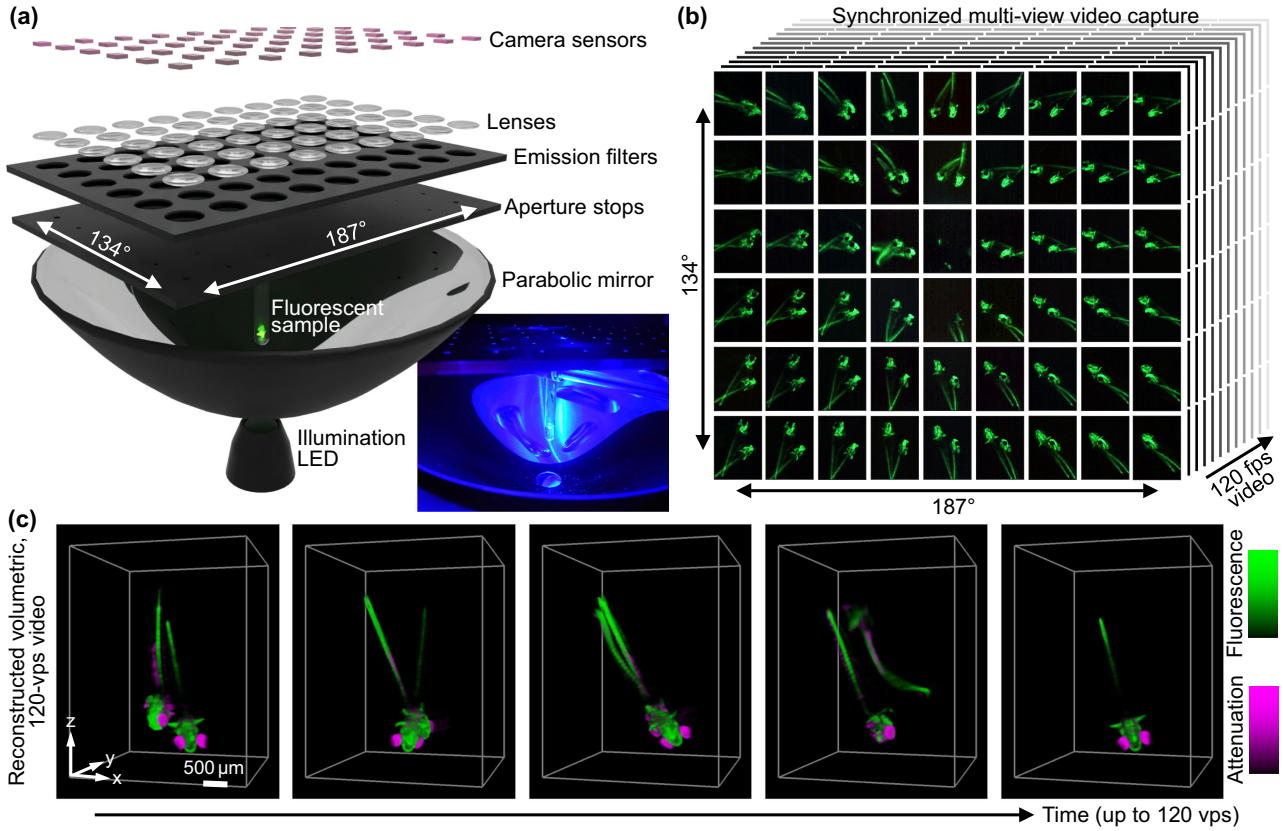

Fig. 1. Overview of ReFLeCT: (a) System design, consisting of an array of 54 multi-view fluorescence imaging systems enabled by a large parabolic mirror objective, with specimen placed at the parabola focus. Inset, photograph of a sample under blue LED illumination, showing the NMR tube in the center, the aperture array above, and the parabolic mirror with the hole below. (b) ReFLeCT captures 54 synchronized multi-view videos, spanning an extremely wide angular range (nearly 2π steradians), at up to 120 fps, limited by the camera readout rate. (c) The ReFLeCT computational reconstruction algorithm reconstructs 3D volumetric videos with two channels, fluorescence and opacity (attenuation coefficient), and a volume rate of up to 120 volumes/sec with near-isotropic 3D resolution. See Visualization 1 for a dynamic overview.

B. System Properties: Angular Coverage, Resolution, Magnification, and Fields of View

The key parameters that determine ReFLeCT's angular coverage, resolution, magnification, and FOV are f_{mirror}, pinhole aperture diameters, and the lateral positions of cameras. Due to the simple, transparent geometry of our system, it is straightforward to establish these relationships.

The multiview angular coverage of ReFLeCT is determined by f_{mirror} and the sensor array spacing and dimensions. In particular, each camera images the sample from a different inclination angle θ, dictated by the radial position r of the sensor across the mirror aperture, according to the following equation [30]:

$$\theta(r) = 2\tan^{-1}\left(\frac{r}{2f_{\text{mirror}}}\right). \tag{1}$$

The outer edge sensors in our system had radial positions ranging from $r = 2.5p = 33.75$ mm (the shorter array dimension) to $r = p\sqrt{2.5^2 + 4^2} \approx 63.58$ mm (the corner cameras), corresponding to $\theta = 67.12°$ and $102.84°$. In total, the multi-angle views of our system span a solid angle of 1.814π or nearly 2π steradians. Note that due to gaps in between the views, our system does not collect light across 2π steradians (see Note 7 in Supplement 1 for discussion on light collection efficiency).

The lateral resolution of the multiview images is determined by the entry position (r) across the mirror aperture and the pinhole aperture diameter. In particular, the object-side effective focal length varies with r like [30]

$$f_{\text{eff}}(r) = f_{\text{mirror}} + \frac{r^2}{4f_{\text{mirror}}}. \tag{2}$$

Using this equation, we calculated the pinhole aperture diameters necessary for a view-angle-independent lateral resolution of ~16 µm, which ranged from 0.8 to 2 mm. Another consequence of the positionally varying effective focal length is that the 54 imaging paths with identical tube lenses cannot simultaneously be 4f systems. Thus, each image has a different magnification, given by

$$M(r) \approx \frac{f_{\text{lens}}}{f_{\text{eff}}(r)}, \tag{3}$$

and a different degree of telecentricity, both of which were pre-calibrated prior to sample reconstruction (Notes 1A and 3 Supplement 1).

For a given camera, the FOV depends not only on magnifications and sensor size but also on the lateral resolution or NAs, which is tuned by the aperture sizes. Assuming the magnification of the image on the sensor is not the limiting factor, the lateral FOV is restricted by the tilt aberrations of the parabolic mirror, which is inversely related to NA or NA^2, depending on r [30]. Notably, the NA^{-2} scaling is analogous to the defocus aberration induced by the DOF. In other words, the mirror aberrations do

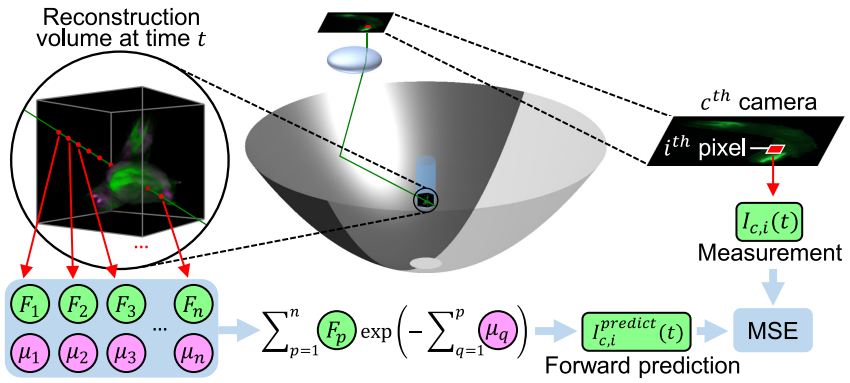

Fig. 2. Overview of forward model of the reconstruction algorithm post system calibration. For clarity, a single chief ray from one pixel (i) of one camera (c) at time t is shown, which propagates through the sample, represented as a two-channel 3D volume. For each time point, the reconstruction volume is sampled at n coordinates to obtain a list of the fluorescence (F) and attenuation (μ). These values are passed through the Beer–Lambert law to predict the measured intensity at the pixel, the difference between that are used to compute the mean square error (MSE), which in turn is minimized via stochastic gradient descent (SGD) with respect to the reconstruction. This reconstruction procedure is repeated for all time points.

not add additional constraints to the FOV over those enforced by the DOF (see details in Ref. [30]). Thus, the optically limited 3D space-bandwidth product (SBP), or effective number of resolvable 3D points, of ReFLeCT increases with decreasing NA, creating a unique trade-off space for future design optimization efforts (see Discussion and Note 7 in Supplement 1).

C. Computational Optical Modeling and Reconstruction

We modeled ReFLeCT's image formation process using a ray-based forward model (Fig. 2), propagating chief rays between the sensors and the sample through all the optical components (similar to Ref. [32]; see also Fig. S1 and Note 2 in Supplement 1 for a detailed description). Although forward models typically start at the sample and terminate at the sensor to predict the measured data, here, we propagated rays in the reverse direction to ensure Cartesian pixel sampling of each video frame. We started propagation of the chief rays corresponding to each pixel of each sensor from the centers of the pupil planes (the stop), where they all intersect, on a per-camera basis. Thereafter, the rays were propagated (Note 2 in Supplement 1; Fig. S1) 1) to the parabolic mirror surface and reflected, 2) to the NMR tube surface and refracted, 3) through the NMR tube wall to the glass–water interface and refracted, and 4) through the water in which the biological sample is freely moving.

In practice, we also accounted for known sources of misalignment parametrically via translation vectors and rotation matrices, such as the relative pose between the camera array and the parabolic mirror and the pose of the NMR tube (Notes 2A and 2C in Supplement 1). While such parametric modeling promoted convergence by offering a good initial guess, it was insufficient to accurately predict our data, so we enriched our ray propagation model nonparametrically using high-order polynomials to account for unknown sources of misalignment and distortions (Note 2B in Supplement 1). For a detailed mathematical treatment of the full ray propagation trajectory, see Note 2 in Supplement 1. These calibration parameters are estimated in a preceding, multi-step calibration procedure (Note 1A in Supplement 1) prior to reconstruction.

Once we obtained the final calibrated rays, specified by position vectors $\mathbf{r}_{c,i}^{\text{sample}}$ and direction unit vectors $\mathbf{u}_{c,i}^{\text{sample}}$, for every pixel i across every camera c, we sampled the dynamic 3D fluorescent object $F(\mathbf{r}, t)$, along the ray trajectories (Fig. 2). To account for attenuation caused by absorption or scattering, we simultaneously modeled a coregistered dynamic 3D attenuation distribution $\mu(\mathbf{r}, t)$ of the object and also sampled voxels along the ray trajectories. To obtain the forward prediction of the pixel i of the camera c, we summed the sampled fluorescence values along the ray, modulated by the attenuation values, in accordance with the Beer–Lambert law (Note 1B in Supplement 1). Finally, we iteratively reconstructed $F(\mathbf{r}, t)$ and $\mu(\mathbf{r}, t)$ minimized the mean square error (MSE) between the forward prediction and the measured pixel intensity using stochastic gradient descent (SGD) for each time point independently (Note 1C in Supplement 1).

3. RESULTS

A. Resolution and FOV Characterization

To characterize the resolution and FOV of our ReFLeCT system, we imaged a sparse distribution of 6 μm green fluorescent beads, embedded in 1% agarose in an NMR tube. We reconstructed the fluorescent beads on an isotropic voxel grid with a voxel size of 8 μm [Figs. 3(a) and 3(b)]. We then segmented the beads and performed fitting using a separable 3D Gaussian model and reported the full widths at half maximum (FWHMs) [Figs. 3(c) and 3(d)]. As expected, the resolution is best at the bottom of the tube (15-20 μm), where the walls form a spherical shell and thus introduce minimal aberration. The resolution gets worse the further away from the bottom of the tube [Fig. 3(c)], due to astigmatism from cylindrical walls and increased distance from the nominal focus of the parabolic mirror, which leads to more defocus and intrinsic tilt aberrations from the parabolic mirror [30]. Nevertheless, the resolution is nearly isotropic, regardless of the position within the FOV [Fig. 3(d)]. The 3D FOV of this implementation of ReFLeCT is thus limited by the minimum acceptable resolution. If we assume a resolution cutoff of ~30 μm, our effective FOV volume would cover ~25 mm^3, while a more generous cutoff would yield ~41 mm^3.

The 3D SBP and spatiotemporal throughput of our system can also be estimated based on Fig. 3. If we assume a 3D FOV volume

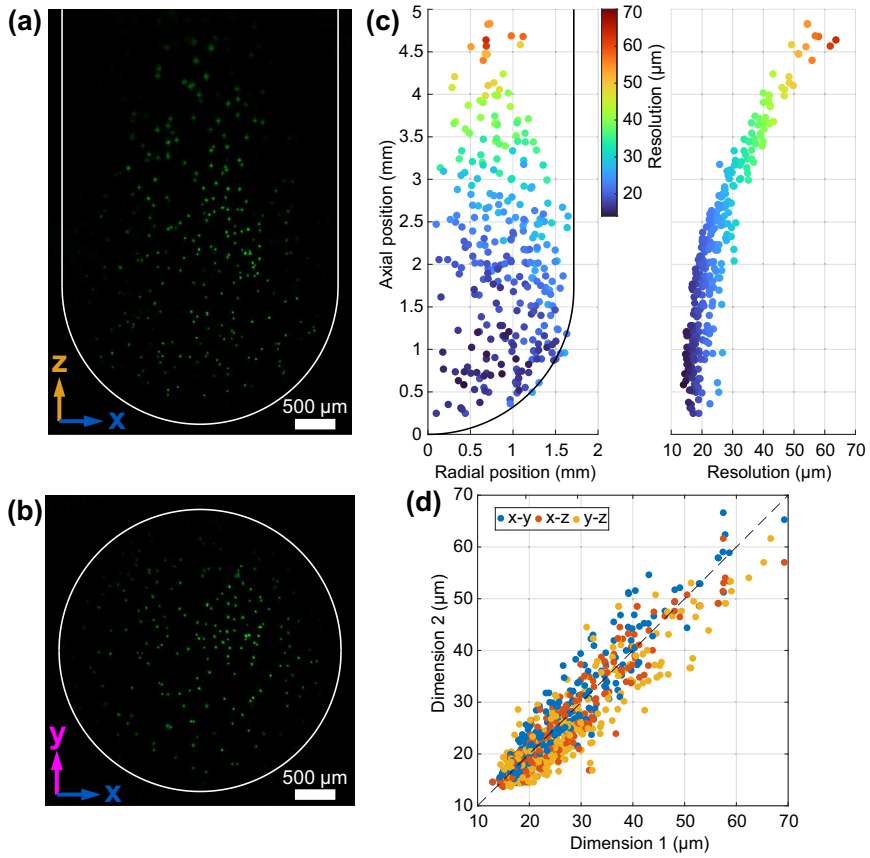

Fig. 3. Resolution and FOV characterization of ReFLeCT with 6 μm green fluorescent beads embedded in 1% agarose. (a) xz projection of volumetric reconstruction. The white line indicates the approximate inner boundary of the NMR tube. (b) xy projection of the reconstruction across the bottom 2.4 mm of the tube. The white circle indicates the approximate inner boundary of straight part of the NMR tube. (c) FWHM of the beads, based on 3D Gaussian fits, of the fluorescent beads plotted across radial and axial positions within the tube. FWHM values are the geometric mean values of the widths in the three dimensions. (d) The x, y, and z FWHM values plotted pairwise against each other, indicating nearly isotropic resolution.

of 25 mm^3 and a resolution of 15-30 μm, Nyquist sampled at 7.5–15 μm, the 3D SBP would range from 25 $mm^3/(7.5\ \mu m)^3$ to 25 $mm^3/(15\ \mu m)^3$ (or 7.4 to 59 megavoxels), which, at 120 volumes per second, bounds the overall spatiotemporal throughout between 0.89 and 7.1 gigavoxels/s.

B. Fruit Fly Larvae (*Drosophila melanogaster*)

Next, we applied ReFLeCT to image several freely moving transgenic fruit flies at late larval stages (third instar wandering larva, WL3), expressing GFP in their muscle cells (*sqh-GFP*, Fig. 4; Visualization 2), pericardial cells (*HandC-GFP*, Fig. 5; Visualization 3), and salivary glands (*NP5169 Gal4 > UAS-GFP-NLS*, Fig. S3; Visualization 4). The volumetric frames of these videos were reconstructed with a voxel size of 16 μm, twice as large as that for the beads (Section 3.1) to boost SNR. Thus, our 3D spatial resolutions are voxel-limited.

From the reconstructed 10 sec, 120 vps video of the *Drosophila* larva with GFP-labeled muscle (*sqh-GFP*), summarized in Fig. 4 and Visualization 2, we observed two peristaltic muscle contraction events, manifesting as a local constriction propagating from the posterior to the anterior of the larva [Fig. 4(a)], lasting about 1 s in duration [38–40]. This localized constriction results in increased localized fluorescence density [Figs. 4(b) and 4(c)(ii)]. During the contractions, the length of the larva also decreases before it increases upon uniform length-wise relaxation [see kymograph in Fig. 4(d), 3.5–4.5 s and 7.5–9 s]. ReFLeCT also enabled us to track the radius of the larva's transverse cross sections along the length of the body and over time (Note 6E in Supplement 1), confirming the radius decrease at the point of constriction as it propagates during the segmental muscle contraction [Fig. 4(e)]. Finally, we also observed jaw motion throughout the contraction[Figs. 4(b) and 4(c)(i); Visualization 2, sagittal and transverse slices].

Next, we reconstructed a 30 vps volumetric video of a freely moving *Drosophila* larva with GFP-labeled pericardial cells [*HandC-GFP*, Fig. 5; Visualization 3]. Since the larva significantly changed its 6D pose (3D position and 3D orientation) throughout the video [Fig. 5(a)], we tracked the larva (Note 6D in Supplement 1) and digitally repositioned and reoriented the virtual camera view so that the larva was always in the same pose, with the pericardial cells facing the virtual camera [Fig. 5(b)]. We have thus defined two coordinate systems: the "world" coordinate system, where z points toward the camera array, and the organism coordinate system, denoted with primes, where x' points from anterior to posterior, y' points from ventral to dorsal, and z' from right to left. As a result, the world coordinate system remains static in Fig. 5(a) and reorients across time in Fig. 5(b), while the opposite is true for organism-centric coordinates. The 6D tracking results are summarized in Fig. 5(e), which shows the 3D position of the larva relative to its initial position and the directions of the x' and y' unit

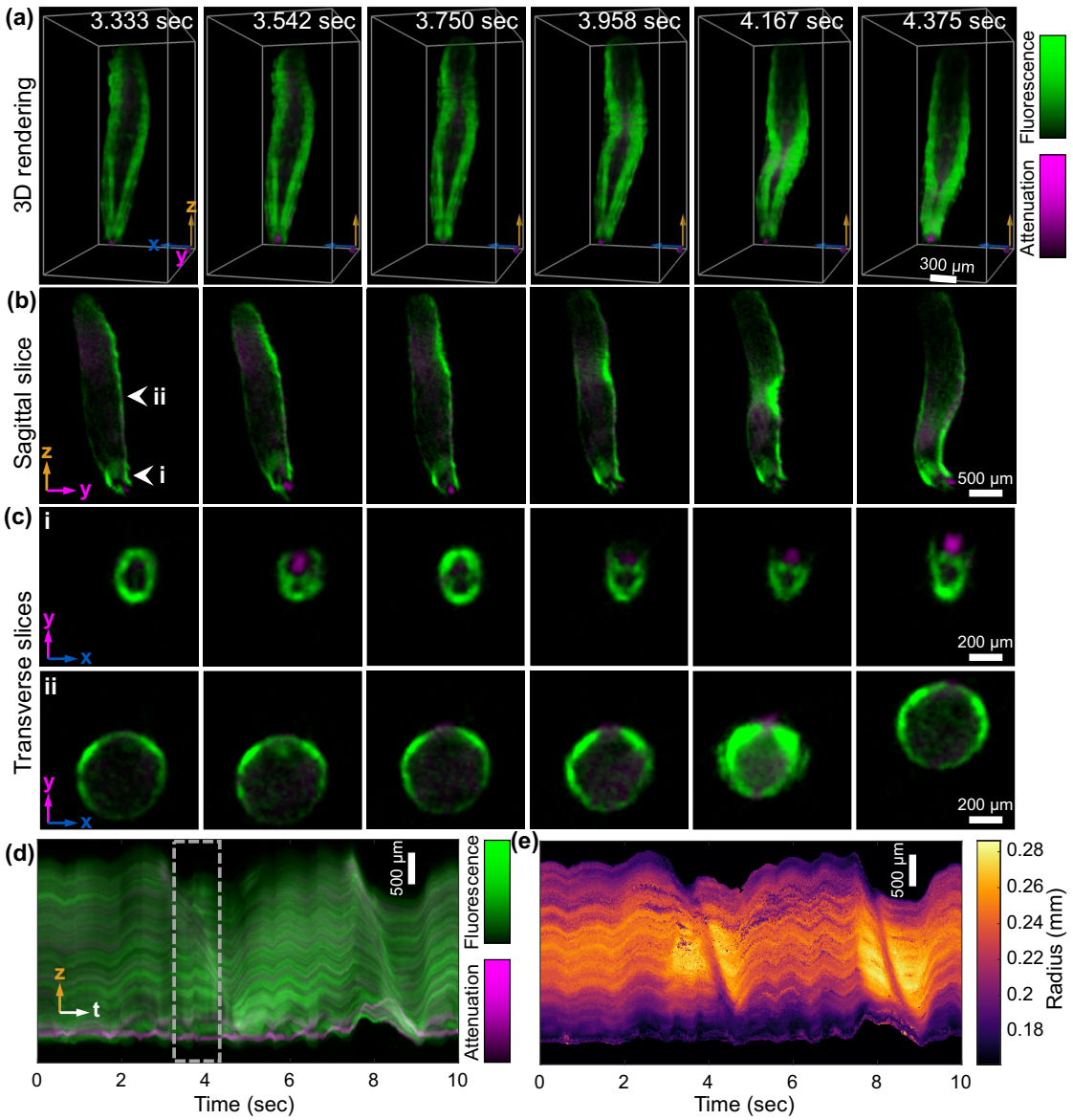

Fig. 4. Volumetric imaging of a freely moving WL3 *Drosophila* larva (*sqh-GFP*) with GFP-labeled myosin at 120 vps. See also the associated Visualization 2. (a) 3D renderings from a fixed perspective of the larva at several time points throughout a segmental muscle contraction. (b) Sagittal (yz) cross section of the larva over time. (c) Two transverse (xz) cross sections (i and ii, indicated by white arrowheads in (b) over time. The first row shows the jaw motion. (d) Summary kymograph of the 10 sec video: 1D max intensity spatial projections across x and y, plotted across time. Dotted box indicates the time range during which the segmental muscle contraction illustrated in a–c occurs. Another contraction occurs around 8 s. (e) Radius of the larva across the length of its body and time.

vectors. The dynamic nature of the larva and its subsequent tracking can also be visualized in the kymographs in Fig. 5(f), where the kymograph post-tracking is more stabilized, with some residual deformations of the longitudinal pericardial cell arrangement due to the larva changing its curvature.

From the tracked larva, we were able to observe dynamic changes in the spacing of the pericardial cells over time [Fig. 5(c)], due to their proximity to the heart [41]. The tomographic imaging capabilities of ReFLeCT also enabled us to observe that the pericardial cells are ∼50 µm below the surface of the larva [Fig. 5(d)].

Finally, we demonstrated multi-organism imaging by reconstructing a 10 sec, 30 vps video of two fruit fly larvae with GFP-labeled salivary glands (*NP5169 Gal4 > UAS-GFP-NLS*, Fig. S3; Visualization 4). The tomographic imaging capabilities of ReFLeCT also recover the hollow tube shape of the salivary glands (Fig. S3d) [42].

C. Zebrafish Larvae (*Danio rerio*)

We also applied ReFLeCT to image several freely swimming zebrafish larvae, including one at 7 days post fertilization (dpf) expressing GFP in plasma membranes in the jaw and notochord (*nfatc:gal4;UAS:GFP-CaaX*) at 120 vps (Fig. 6; Visualization 5), one at 4 dpf expressing GFP in the heart (*cmlc2:GFP*) at 30 vps (Fig. 7; Visualization 7), and another at 6 dpf expressing GFP in neuronal plasma membranes (*gad1b:gal4;UAS:GFP-CaaX*) at 120 vps (Visualization 6). The reconstruction voxel size (16 µm)

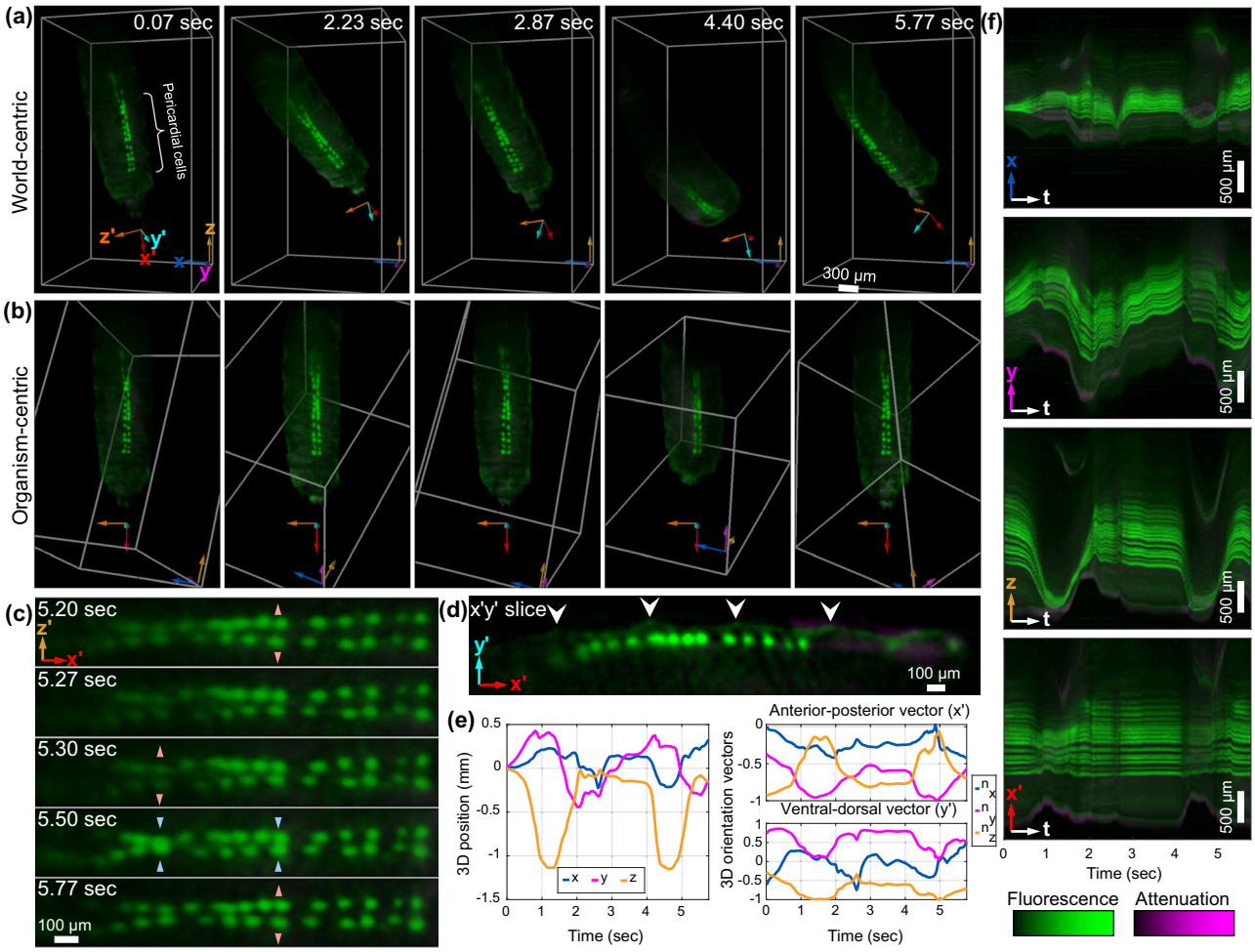

Fig. 5. Volumetric imaging of a freely moving WL3 fruit fly larva (*HandC-GFP*) with GFP-labeled pericardial cells at 30 vps. See also the associated Visualization 3. (a) 3D renderings from a fixed perspective of the larva at several time points. The primed coordinate system is relative to the larva, while the unprimed coordinate system is of the imaging system ("world"). (b) 3D renderings at the same time points as in (a) but with a perspective locked onto the larva. (c) Close-up of the pericardial cells at five time points. Arrowheads indicate when a pair of pericardial cells are moving closer to each other or further away. (d) Sagittal cross section through the larva, showing that the pericardial cells are ∼50 µm below the surface. White arrowheads indicate the segmental furrows interleaving the body segments. (e) 6D pose of the larva over time. Left plot is of its 3D position, referenced to its initial position. Right plots show 3D orientation, represented by two larva-centric unit vector axes (x' and y', shown in a). (f) Visualization of the 4D data (3D + time), max-intensity-projected down to 2D kymographs (xt, yt, and zt). The fourth kymograph ($x't$) projects across the *larva*'s axes (y' and z'), with residual motion due to the larva changing its curvature.

and larva-centric coordinate systems are the same as the ones we used for fruit fly larvae (Section 3.2).

Figure 6(a) shows a few reconstructed volumes of the 120 vps video of the 7 dpf zebrafish larva (*nfatc:gal4;UAS:GFP-CaaX*). Here, not only does the green fluorescence provide useful contrast but also the attenuation channel (magenta) highlights the eyes of the larva as well as the pigmentation patterns spanning the length of the body. Figure S4 also confirms the importance of modeling sample attenuation by examining the forward predictions. Since the zebrafish larva rapidly changed its position and orientation as it swam, we performed 6D pose tracking of the head using only the green fluorescence channel (see Note 6D in Supplement 1). The tracking data are summarized in Figs. 6(c)–6(e), showing the 3D head position and the larva's ventral–dorsal (x') and right–left (z') axes orientation plotted against time. Using these tracking data, such as with *Drosophila* larva (Fig. 5, Section 3.2), we dynamically changed the virtual camera perspective throughout the reconstructed video so that the fish head appears static [Fig. 6(b)].

Since we tracked the 6D pose and coregistered the larva from all time points, we were able to track many other properties of the larva [Figs. 6(f)–6(l)]. One property was the 3D position of the tail tip [Fig. 6(f)], which moves primarily in the z' axis (left–right), and occasionally produces large strokes that result in the tail getting close to the head (near 0.4 and 1.6 s). We also tracked the orientation of the left and right pectoral fins [Figs. 6(g) and 6(h)], as well as the gaze of both eyes based on the attenuation channel [Figs. 6(i) and 6(j)]. Note that the gaze oscillates along with the rest of the body, possibly due to the vestibulo-ocular reflex (VOR) [43,44]. These oscillations are not an artifact of volume registration, as only the fluorescence channel was used for registration. We also tracked the jaw motion [Fig. 6(k)] and the heartbeat of the fish [Fig. 6(l)], which are both visible in Fig. 6(b) (and Visualization 5).

Additionally, we imaged a 4 dpf zebrafish larva at 30 vps, with GFP labeling localized exclusively to the heart [*cmlc2:GFP*, Fig. 7(a); Visualization 7]. The kymographs in Fig. 7(c) show the trajectories of the freely swimming larva. Upon 6D pose tracking

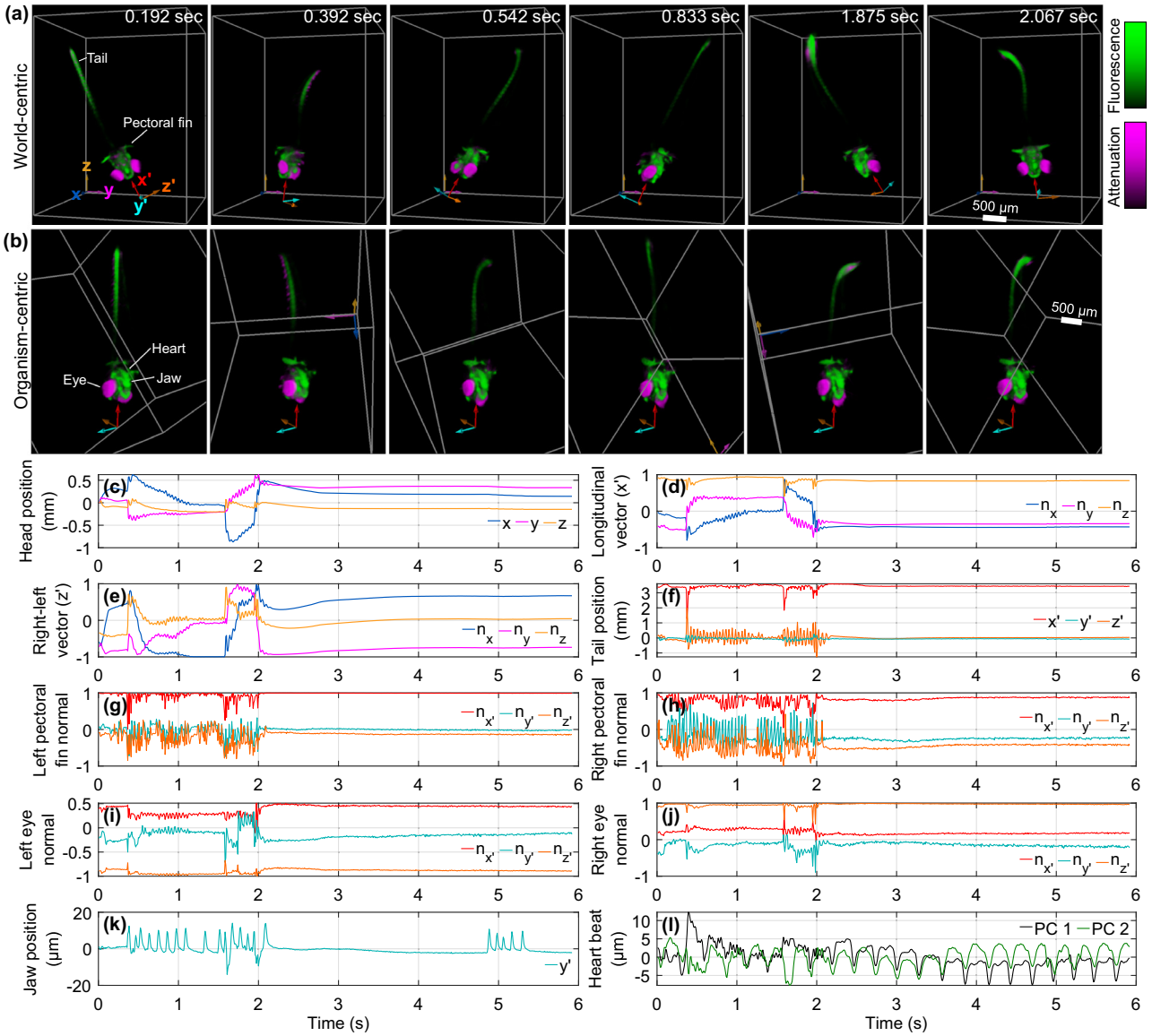

Fig. 6. Volumetric imaging of a freely moving 7 dpf zebrafish larva (*nfatc:gal4;UAS:GFP-CaaX*) at 120 vps, with GFP expression in plasma membranes in the jaw and notochord. See also the associated Visualization 5. (a) 3D renderings of the larva from a fixed perspective over time. The primed axes are relative to the larva, while the unprimed axes are of the imaging system ("world"). (b) 3D renderings, perspective-locked to the larva's tracked head. (c–k) Various tracked properties of the fish over time. The color-coding matches that of the axes in (a), depending on whether they reference the larva's or the world coordinate system. (c) 3D position of the larva's head over time, relative to its initial position. (d–e) The 3D orientation of the larva over time, represented by the components of the unit vectors pointing from its anterior to posterior (x') and its right to left (z'). (f) Tail position of the larva over time, relative to the tracked head position. (g–h) Orientation of the left and right pectoral fins, respectively, represented as the unit vector normal to the fin. (i–j) Gaze direction of the left and right eyes, respectively. (k) Jaw position over time. (l) Tracked heartbeat over time, represented as the first two principal components (PCs) of its motion.

[Figs. 7(d)–(f)] and volumetric coregistration, we were able to visualize the atrium and ventricle of the heart [Fig. 7(b)], including the phase offset delay between their contractions [Fig. 7(g)].

4. DISCUSSION

Reflective Fourier light field computed tomography (ReFLeCT) is a new high-throughput computational imaging technique for tomographic 3D video over $>25-\text{mm}^3$ volumes at up to 15–20 µm isotropic 3D spatial resolution [Fig. 3] and 120 Hz synchronized frame rates, culminating in multi-gigavoxel/sec dynamic volume throughputs. Using the high speeds and large viewing volumes of ReFLeCT, we demonstrated behavioral imaging of freely moving organisms (*Drosophila* and zebrafish larvae) without the need for anesthesia or restraint, thus avoiding confounding effects on organism behavior and physiology [24,45,46]. To elucidate and quantify their unconstrained 3D behavior, we developed a 6D pose tracking and registration algorithm for perspective-locking onto the animal. With this software, we were able to track and quantify physiological dynamics such as heartbeat, eye gaze, and fin motion, all in full 3D, which otherwise require organism immobilization for longitudinal measurement. ReFLeCT also opens up the possibility of high-speed volumetric video observation of behavioral interactions across multiple

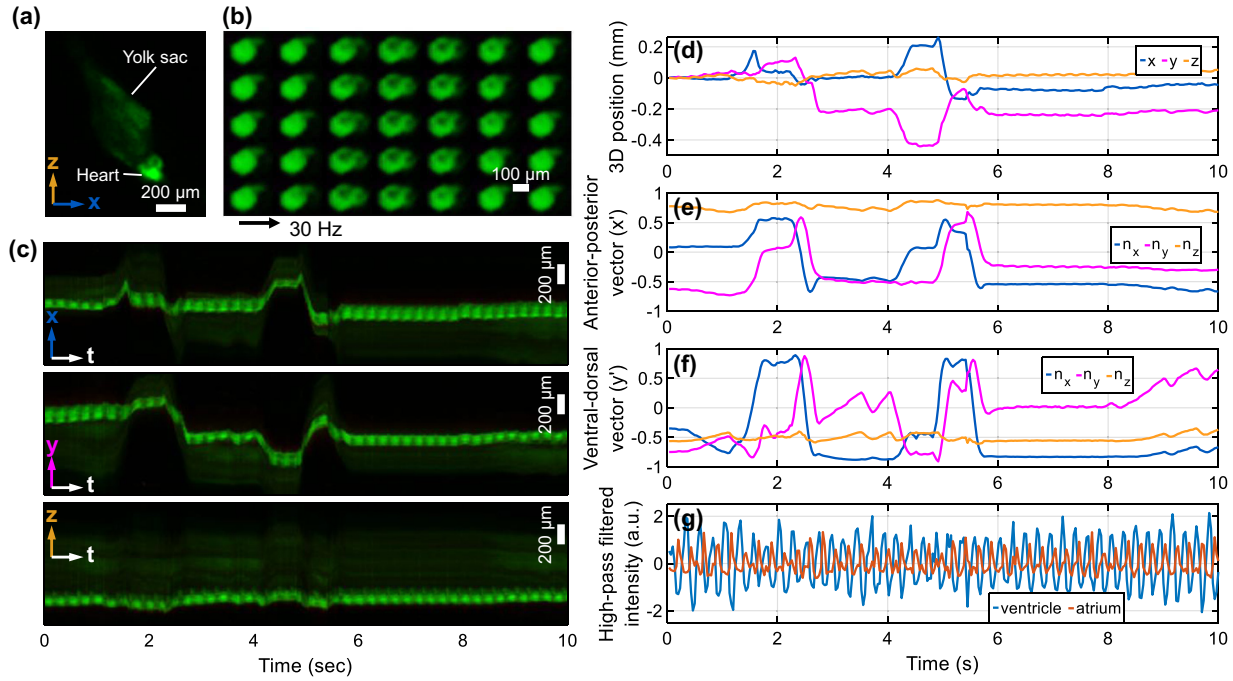

Fig. 7. Volumetric imaging of a 4 dpf zebrafish larva (*cmlc2:GFP*) expressing GFP in the heart, at 30 vps. See also the associated Visualization 7. (a) xz max projection of 3D reconstruction at one time point. (b) Six sequential cardiac cycles, showing its two heart chambers (ventricle and atrium). The time difference between sequential images is 33 ms. (c) 1D max projections across two of the three spatial dimensions, plotted across time. The $x/y/z$ axes are relative to the imaging system (i.e., not the fish). (d) The 3D position of the fish over time, relative to its position at the start of the video. (e–f) The 3D orientation of the fish over time, represented by the unit vectors pointing from head to tail (e) and from its ventral to dorsal sides (f). (g) Temporally high-pass filtered fluorescence intensity of the ventricle and atrium.

organisms—a new capability with relevance in neuroscience and developmental biology [33–37].

We believe ReFLeCT is a significant step forward toward bridging the gap between micro-scale fluorescence imaging and macro-scale behavioral observation. In particular, at the cost of the high spatial resolutions achievable by light sheets and other forms of microscopy, ReFLeCT can more readily scale to larger FOVs and higher volume rates. Specifically, the higher the NA of refractive objectives commonly used in microscopy, the smaller the FOV. Further, the cameras used in light sheet microscopy need to be much faster than the desired volume rate, while the volume rate of ReFLeCT is exactly the camera frame rate.

However, there are many avenues for improvement, as ReFLeCT's resolution and light collection efficiency (Note 7 in Supplement 1) are comparatively worse than those of existing microscopy approaches. While the resolution of our prototype is isotropic and sufficient for behavioral imaging, higher resolution may be necessary for a variety of functional imaging applications, in particular to monitor neural activity. Since ReFLeCT's resolution is tied to the DOF of each imaging module and therefore its total volume of view (Note 7 in Supplement 1), it would be straightforward to design new ReFLeCT systems that capture across smaller volumes at higher resolution (and conversely, larger volumes at lower resolution). Alternatively, one can employ DOF extension strategies [28,47–50] to achieve higher resolution while maintaining a large volume of view, or introduce refractive elements [31,51] to correct the mirror aberrations that limit the FOV [30]. Our approach is also complementary to 3D active organism tracking approaches [24], which would expand the effective 3D FOV. Increasing the resolution by expanding the aperture sizes of each imaging module or packing more imaging modules would also increase the overall measurement SNR by allowing greater light collection efficiency (Note 7 in Supplement 1). Our current implementation has other inefficiencies, stemming from the use of Bayer sensors (∼50% loss) and sensor downsampling (75% and 93.75% loss for 2× and 4× downsampling, respectively), which would be straightforward to address. It is also direct to envision multi-wavelength excitation and emission filtering strategies for multi-channel fluorescence video sampling with ReFLeCT, which could increase cellular-level specificity and allow ratiometric analyses. Finally, as we begin to design behavioral experiments with ReFLeCT, it would be straightforward to introduce visual stimuli to the organism by introducing a dichroic mirror in the excitation or emission paths, or by making the parabolic mirror itself a dichroic.

While the spatiotemporal throughput of our current ReFLeCT design is limited by the data transfer rate from our sensors to the computer to ∼5 GB/sec [52,53], improvements to our data transfer architecture and the creation of image sensor arrays with faster camera sensors could enable applications in imaging fluorescent voltage sensors to monitor neural activity [54] and capture high-speed behaviors (e.g., rapid zebrafish locomotion during swim bouts [55] or kinematics during seizure activity [56]), potentially simultaneously across multiple organisms. On the computational backend, to handle such increased spatiotemporal data throughputs, we could adapt neural radiance fields (NeRFs) [57] and recent advances in accelerating optimization speed [58], extending them to implicit 4D representations [59–63]. Moreover, reparameterizing tomographic reconstructions as outputs of neural networks can offer regularizing effects [64,65]. With such

improvements, ReFLeCT could readily record high-speed 3D fluorescent dynamics within a variety of alternative organisms (e.g., *C. elegans* [66], jellyfish [67]), 3D cellular models (e.g., neural activity within cerebral organoids [68]), and alternative setups (e.g., 3D flow cytometry [69]) to open up new avenues for future scientific exploration.

Funding. National Institute of Environmental Health Sciences (R44OD024879); National Cancer Institute (R44CA250877); National Institute of Biomedical Imaging and Bioengineering (R43EB030979); National Institute of General Medical Sciences (R01GM150666, R01GM118447, R01GM140138); National Science Foundation (2036439); Duke-Coulter Translational Partnership Grant; American Heart Association (23POST1013432); Schmidt Science Fellows.

Disclosures. KCZ: Ramona Optics Inc. (C). MH: Ramona Optics Inc. (F, I, P, S). RH: Ramona Optics Inc. (F, I, P, S). KCZ, RH: Duke University (P).

Data availability. The Python code for 4D reconstruction and interactive visualization is available at [70] and [71], respectively. Data underlying the results of this paper are available at [72].

Supplemental document. See Supplement 1 for supporting content.

REFERENCES

1. J. Pawley, *Handbook of biological confocal microscopy*, Vol. **236** (Springer Science & Business Media, 2006).
2. W. R. Zipfel, R. M. Williams, and W. W. Webb, "Nonlinear magic: multiphoton microscopy in the biosciences," Nat. Biotechnol. **21**, 1369–1377 (2003).
3. J. Oreopoulos, R. Berman, and M. Browne, "Spinning-disk confocal microscopy: present technology and future trends," Methods Cell Biol. **123**, 153–175 (2014).
4. J. L. Wu, Y. Q. Xu, J. J. Xu, *et al.*, "Ultrafast laser-scanning time-stretch imaging at visible wavelengths," Light Sci. Appl. **6**, e16196 (2017).
5. M. B. Ahrens, M. B. Orger, D. N. Robson, *et al.*, "Whole-brain functional imaging at cellular resolution using light-sheet microscopy," Nat. Methods **10**, 413–420 (2013).
6. B.-C. Chen, W. R. Legant, K. Wang, *et al.*, "Lattice light-sheet microscopy: imaging molecules to embryos at high spatiotemporal resolution," Science **346**, 1257998 (2014).
7. R. K. Chhetri, F. Amat, Y. Wan, *et al.*, "Whole-animal functional and developmental imaging with isotropic spatial resolution," Nat. Methods **12**, 1171–1178 (2015).
8. V. Voleti, K. B. Patel, W. Li, *et al.*, "Real-time volumetric microscopy of in vivo dynamics and large-scale samples with SCAPE 2.0," Nat. Methods **16**, 1054–1062 (2019).
9. B. Yang, M. Lange, A. Millett-Sikking, *et al.*, "Daxi—high-resolution, large imaging volume and multi-view single-objective light-sheet microscopy," Nat. Methods **19**, 461–469 (2022).
10. F. O. Fahrbach, F. F. Voigt, B. Schmid, *et al.*, "Rapid 3D light-sheet microscopy with a tunable lens," Opt. Express **21**, 21010–21026 (2013).
11. M. Mickoleit, B. Schmid, M. Weber, *et al.*, "High-resolution reconstruction of the beating zebrafish heart," Nat. Methods **11**, 919–922 (2014).
12. S. Daetwyler, B.-J. Chang, B. Chen, *et al.*, "Mesoscopic oblique plane microscopy via light-sheet mirroring," Optica **10**, 1571–1581 (2023).
13. R. Singh, K. Subramanian, R. M. Power, *et al.*, "Oblique plane microscope for mesoscopic imaging of freely moving organisms with cellular resolution," Opt. Express **31**, 2292–2301 (2023).
14. Z. Wang, J. Zhang, P. Symvoulidis, *et al.*, "Imaging the voltage of neurons distributed across entire brains of larval zebrafish," bioRxiv2023).
15. J. Sharpe, U. Ahlgren, P. Perry, *et al.*, "Optical projection tomography as a tool for 3D microscopy and gene expression studies," Science **296**, 541–545 (2002).
16. V. Lauer, "New approach to optical diffraction tomography yielding a vector equation of diffraction tomography and a novel tomographic microscope," J. Microsc. **205**, 165–176 (2002).
17. S. Chowdhury, M. Chen, R. Eckert, *et al.*, "High-resolution 3D refractive index microscopy of multiple-scattering samples from intensity images," Optica **6**, 1211–1219 (2019).
18. A. Matlock and L. Tian, "High-throughput, volumetric quantitative phase imaging with multiplexed intensity diffraction tomography," Biomed. Opt. Express **10**, 6432–6448 (2019).
19. C. Darling, S. P. Davis, S. Kumar, *et al.*, "Single-shot optical projection tomography for high-speed volumetric imaging of dynamic biological samples," J. Biophotonics **16**, e202200232 (2023).
20. D. Huang, E. A. Swanson, C. P. Lin, *et al.*, "Optical coherence tomography," Science **254**, 1178–1181 (1991).
21. K. C. Zhou, R. Qian, A. H. Dhalla, *et al.*, "Unified k-space theory of optical coherence tomography," Adv. Opt. Photonics **13**, 462–514 (2021).
22. T. Klein and R. Huber, "High-speed oct light sources and systems," Biomed. Opt. Express **8**, 828–859 (2017).
23. M. Levoy, R. Ng, A. Adams, *et al.*, "Light field microscopy," in *ACM SIGGRAPH 2006 Papers* (2006), pp. 924–934.
24. L. Cong, Z. Wang, Y. Chai, *et al.*, "Rapid whole brain imaging of neural activity in freely behaving larval zebrafish (*Danio rerio*)," elife **6**, e28158 (2017).
25. C. Guo, W. Liu, X. Hua, *et al.*, "Fourier light-field microscopy," Opt. Express **27**, 25573–25594 (2019).
26. K. Yanny, N. Antipa, W. Liberti, *et al.*, "Miniscope3D: optimized single-shot miniature 3D fluorescence microscopy," Light Sci. Appl. **9**, 1–13 (2020).
27. J. Wu, Z. Lu, D. Jiang, *et al.*, "Iterative tomography with digital adaptive optics permits hour-long intravital observation of 3D subcellular dynamics at millisecond scale," Cell **184**, 3318–3332 (2021).
28. Y. Zhang, Y. Wang, M. Wang, *et al.*, "Multi-focus light-field microscopy for high-speed large-volume imaging," PhotoniX **3**, 30 (2022).
29. Z. Wang, R. Zhao, D. A. Wagenaar, *et al.*, "Kilohertz volumetric imaging of in-vivo dynamics using squeezed light field microscopy," bioRxiv, pp. 2024–03 (2024).
30. K. C. Zhou, A. H. Dhalla, R. P. McNabb, *et al.*, "High-speed multiview imaging approaching 4pi steradians using conic section mirrors: theoretical and practical considerations," J.Opt.Soc.Am A **38**, 1810–1822 (2021).
31. F. F. Voigt, A. M. Reuss, T. Naert, *et al.*, "Reflective multi-immersion microscope objectives inspired by the Schmidt telescope," Nat. Biotechnol. **42**, 65–71 (2024).
32. K. C. Zhou, R. P. McNabb, R. Qian, *et al.*, "Computational 3D microscopy with optical coherence refraction tomography," Optica **9**, 593–601 (2022).
33. Z. Durisko, R. Kemp, R. Mubasher, *et al.*, "Dynamics of social behavior in fruit fly larvae," PLoS One **9**, e95495 (2014).
34. J. D. Mast, C. M. De Moraes, H. T. Alborn, *et al.*, "Evolved differences in larval social behavior mediated by novel pheromones," Elife **3**, e04205 (2014).
35. E. Dreosti, G. Lopes, A. R. Kampff, *et al.*, "Development of social behavior in young zebrafish," Front. Neural Circuits **9**, 39 (2015).
36. B. B. Anderson, A. Scott, and R. Dukas, "Social behavior and activity are decoupled in larval and adult fruit flies," Behav. Ecol. **27**, 820–828 (2016).
37. N. Otto, B. Risse, D. Berh, *et al.*, "Interactions among Drosophila larvae before and during collision," Sci. Rep. **6**, 31564 (2016).
38. S. Lahiri, K. Shen, M. Klein, *et al.*, "Two alternating motor programs drive navigation in *Drosophila* larva," PloS one **6**, e23180 (2011).
39. E. S. Heckscher, S. R. Lockery, and C. Q. Doe, "Characterization of Drosophila larval crawling at the level of organism, segment, and somatic body wall musculature," J. Neurosci. **32**, 12460–12471 (2012).
40. H. Kohsaka, E. Takasu, T. Morimoto, *et al.*, "A group of segmental premotor interneurons regulates the speed of axial locomotion in Drosophila larvae," Curr. Biol. **24**, 2632–2642 (2014).
41. B. Rotstein and A. Paululat, "On the morphology of the *Drosophila* heart," J. Cardiovasc. Dev. Dis. **3**, 15 (2016).
42. B. E. Kerman, A. M. Cheshire, and D. J. Andrew, "From fate to function: the *Drosophila* trachea and salivary gland as models for tubulogenesis," Differentiation **74**, 326–348 (2006).
43. W. Mo, F. Chen, A. Nechiporuk, *et al.*, "Quantification of vestibular-induced eye movements in zebrafish larvae," BMC Neurosci. **11**, 1–11 (2010).
44. I. H. Bianco, L.-H. Ma, D. Schoppik, *et al.*, "The tangential nucleus controls a gravito-inertial vestibulo-ocular reflex," Curr. Biol. **22**, 1285–1295 (2012).
45. D. Grover, T. Katsuki, and R. J. Greenspan, "Flyception: imaging brain activity in freely walking fruit flies," Nat. Methods **13**, 569–572 (2016).
46. R. E. Johnson, S. Linderman, T. Panier, *et al.*, "Probabilistic models of larval zebrafish behavior reveal structure on many scales," Curr. Biol. **30**, 70–82 (2020).

47. G. Häusler, "A method to increase the depth of focus by two step image processing," Opt. Commun. **6**, 38–42 (1972).
48. E. R. Dowski and W. T. Cathey, "Extended depth of field through wavefront coding," Appl. Opt. **34**, 1859–1866 (1995).
49. S. Abrahamsson, S. Usawa, and M. Gustafsson, "A new approach to extended focus for high-speed high-resolution biological microscopy," Proc. SPIE **6090**, 60900N (2006).
50. R. Tomer, M. Lovett-Barron, I. Kauvar, *et al.*, "SPED light sheet microscopy: fast mapping of biological system structure and function," Cell **163**, 1796–1806 (2015).
51. P. J. Keller, D. A. Flickinger, and B. Wang, "Catadioptric microscopy," US Patent App.17/779,076 (05 January2023).
52. M. Harfouche, K. Kim, K. C. Zhou, *et al.*, "Imaging across multiple spatial scales with the multi-camera array microscope," Optica **10**, 471–480 (2023).
53. K. C. Zhou, M. Harfouche, C. L. Cooke, *et al.*, "Parallelized computational 3D video microscopy of freely moving organisms at multiple gigapixels per second," Nat. Photonics **17**, 442–450 (2023).
54. T. Knöpfel and C. Song, "Optical voltage imaging in neurons: moving from technology development to practical tool," Nat. Rev. Neurosci. **20**, 719–727 (2019).
55. K. E. Severi, R. Portugues, J. C. Marques, *et al.*, "Neural control and modulation of swimming speed in the larval zebrafish," Neuron **83**, 692–707 (2014).
56. S. Baraban, M. Dinday, and G. Hortopan, "Drug screening in Scn1a zebrafish mutant identifies clemizole as a potential Dravet syndrome treatment," Nat. Commun. **4**, 2410 (2013).
57. B. Mildenhall, P. P. Srinivasan, M. Tancik, *et al.*, "Nerf: representing scenes as neural radiance fields for view synthesis," in *European Conference on Computer Vision* (Springer, 2020), pp. 405–421.
58. T. Müller, A. Evans, C. Schied, *et al.*, "Instant neural graphics primitives with a multiresolution hash encoding," ACM Trans. Graph. **41**, 102:1–102:15 (2022).
59. W. Gan, H. Xu, Y. Huang, *et al.*, "V4d: Voxel for 4D novel view synthesis," arXiv (2022).
60. S. Fridovich-Keil, G. Meanti, F. R. Warburg, *et al.*, "K-planes: explicit radiance fields in space, time, and appearance," in *Proceedings of the IEEE/CVF Conference on Computer Vision and Pattern Recognition* (2023), pp. 12479–12488.
61. A. Cao and J. Johnson, "Hexplane: A fast representation for dynamic scenes," in *Proceedings of the IEEE/CVF Conference on Computer Vision and Pattern Recognition (CVPR)* (2023), pp. 130–141.
62. R. Shao, Z. Zheng, H. Tu, *et al.*, "Tensor4d: efficient neural 4d decomposition for high-fidelity dynamic reconstruction and rendering," in *Proceedings of the IEEE/CVF Conference on Computer Vision and Pattern Recognition (CVPR)* (2023), pp. 16632–16642.
63. G. Wu, T. Yi, J. Fang, *et al.*, "4d gaussian splatting for real-time dynamic scene rendering," in *Proceedings of the IEEE/CVF Conference on Computer Vision and Pattern Recognition* (2024), pp. 20310–20320.
64. K. C. Zhou and R. Horstmeyer, "Diffraction tomography with a deep image prior," Opt. Express **28**, 12872–12896 (2020).
65. R. Liu, Y. Sun, J. Zhu, *et al.*, "Recovery of continuous 3D refractive index maps from discrete intensity-only measurements using neural fields," Nat. Mach. Intell. **4**, 781–791 (2022).
66. L. Morales-Curiel, A. Gonzalez, G. Castro-Olvera, *et al.*, "Volumetric imaging of fast cellular dynamics with deep learning enhanced bioluminescence microscopy," Commun. Biol. **5**, 1330 (2022).
67. B. Weissbourd, T. Momose, A. Nair, *et al.*, "A genetically tractable jellyfish model for systems and evolutionary neuroscience," Cell **184**, 5854–5868.e20 (2021).
68. D. Hendriks, A. Pagliaro, F. Andreatta, *et al.*, "Human fetal brain self-organizes into long-term expanding organoids," Cell **187**, 712–732 (2024).
69. X. Hua, K. Han, B. Mandracchia, *et al.*, "Light-field flow cytometry for high-resolution, volumetric and multiparametric 3D single-cell analysis," Nat Commun. **15**, 1975 (2024).
70. https://github.com/kevinczhou/ReFLeCT.
71. https://github.com/kevinczhou/ReFLeCT-4D-visualization.
72. K. Zhou, C. Cook, A. Chakraborty, *et al.*, "Data from: High-speed 4D fluorescence light field tomography of whole freely moving organisms," Duke Research Data Repository (2025), https://doi.org/10.7924/r4zs30t4h.